

PAPER

Cite this: *J. Mater. Chem. A*, 2022, **10**, 12977

Crystalline microporous small molecule semiconductors based on porphyrin for high-performance chemiresistive gas sensing†

Wei-Hua Deng,^{‡abc} Liang He,^{‡abc} Er-Xia Chen,^{ac} Guan-E. Wang,^a Xiao-Liang Ye,^a Zhi-Hua Fu,^a Qipu Lin^{‡abc} and Gang Xu^{‡abc}

Organic small molecule semiconductor (OSMS) microporous crystals with strong π - π interactions are rare but have great potential in applications requiring both excellent mass and charge transport. To obtain such a microporous structure, effective molecule design and control over the packing of the OSMS are necessary but still challenging. Herein, we report three *meso*-tetrakis (4-carboxyphenyl) porphyrin (TCPP) based porous OSMS materials, **1**, **2** and **3**, whose porosity and π - π interactions among TCPPs were modulated by varying the H-bonding linkage nodes. The relationship among the hydrogen bonding structure, packing mode and sensing performances has been carefully studied. With the largest overlap between porphyrin rings and strongest face-to-face π - π interactions in the prepared compound, **1** showed the best performances. Moreover, it also represents the first RT NO₂ chemiresistive sensing material that simultaneously achieved an experimental limit of detection as low as 20 ppb and a time of recovery as short as 0.6 min. This work revealed the key role of H-bonding linkage node in constructing a microporous OSMS and provides a new type of high-performance rt chemiresistive gas sensing material.

Received 24th December 2021
Accepted 20th May 2022

DOI: 10.1039/d1ta10945f

rsc.li/materials-a

Introduction

Organic small molecule semiconductors (OSMSs) with large π -conjugated systems, such as pentacene, rubrene, phthalocyanine and porphyrin, are of great interest because of their modifiable molecular structures and unique optical/electrical properties.¹⁻⁴ OSMSs have great potential in field-effect transistors (FETs), light-emitting diodes, solar cells, organic radical batteries, and chemical sensors.⁵⁻⁹ In OSMS crystals, molecules are retained in stacks by relatively weak interactions, *e.g.*, π - π , van der Waals and electrostatic interactions.¹⁰ These interactions are non-directional, which poses a challenge for a desired crystal structure through a topology-induced synthesis.¹¹ Since charge transport in OSMSs normally depends on the hopping probability of the carriers from one molecule to another, different molecule packing features, such as intermolecular

separation and intermolecular overlap will result in different semiconducting properties and device performances.¹² Thus, much effort has been devoted to controlling the long-range packing modes of OSMSs.¹³ If a microporous structure could be realized by modulating the packing, OSMSs would have large inner surfaces and penetrability. The combination of porosity and semiconducting properties could open a new dimension in advanced electronic applications, *e.g.*, liquid-gated FETs, voltage-gated ion channels, microfluidic chips, and various chemical sensors.¹⁴⁻¹⁶ Hydrogen bonds among molecules have been found to be useful in the construction of crystalline microporous materials.¹⁷⁻¹⁹ Owing to the reversible and flexible characteristics of H-bonding connections, materials with multiple H-bonds exhibit many unique advantages including high crystallinity, large surface areas, mild synthetic conditions, and easy healing and purification.^{20,21} Taking this strategy, many microporous OSMSs have been successfully prepared.²² However, electronic devices constructed with crystalline microporous OSMSs have been reported rarely to date.²³

Chemiresistive gas sensors are very useful for monitoring pollution in the atmosphere and are used in fields such as industrial production, environmental protection, and health care.^{24,25} However, traditional inorganic chemiresistive gas sensing materials are still limited by low sensitivity at room temperature (rt) and poor selectivity.²⁶ Compared with inorganic materials, organic materials, such as OSMSs, possess

^aState Key Laboratory of Structural Chemistry, Fujian Institute of Research on the Structure of Matter, Chinese Academy of Sciences, Fuzhou, Fujian 350002, China. E-mail: lingqipu@fjirsm.ac.cn; gxu@fjirsm.ac.cn

^bUniversity of Chinese Academy of Sciences, Beijing 100049, China

^cFujian Science & Technology Innovation Laboratory for Optoelectronic Information of China, Fuzhou, Fujian 350108, China

† Electronic supplementary information (ESI) available: Experimental details and characterization data as well as the crystallographic data of **1** and **2**. CCDC 2127390 for **2**. For ESI and crystallographic data in CIF or other electronic format see <https://doi.org/10.1039/d1ta10945f>

‡ These authors contributed equally to this work.

more flexibility in structure design to obtain high sensitivity at rt and selectivity.²³ Moreover, microporous OSMSs can provide a higher specific surface area and functionalized pore wall to further improve the sensing performances due to the improved mass and charge transport. However, this field is still at its infancy. Jiang and co-workers report the first and also the only example of a microporous OSMS sensor, which shows very promising rt NO₂ sensing.²³ To further improve the sensing performances for practical applications, the relationship among the hydrogen bonding structure, packing structure and sensing performances is extremely desired.

Herein, we explored the packing mode of *meso*-tetrakis (4-carboxyphenyl) porphyrin (TCPP). It has a cross shape and four arms, each terminating in a carboxyl group, which is a favored geometry for constructing a hydrogen bonding network in a given topology. Single-crystal X-ray crystallography revealed that three different types of H-bonding linkage nodes were formed in **1**, **2** and **3**. Different linkage nodes modulated the packing structure of TCPP with different porosities and π - π interactions. The packing modes of porphyrin that significantly influence the chemiresistive sensing performances were studied. As a result, **1** showed one of the highest overall performances among all reported rt NO₂ sensing materials.

Results and discussion

As shown in Fig. S1,[†] microporous **1** and **2** were synthesized by solvothermal recrystallization of TCPP in a solution of *N,N*-dimethylformamide (DMF)/acetonitrile (MeCN) at different temperatures (see the Experimental section for details). The non-porous **3** was prepared by a reported method.²⁷ The structures of **1**, **2** and **3** were determined by single crystal X-ray diffraction (XRD) crystallography, powder XRD with Rietveld fitting (Tables S2 and S3[†]) and Fourier transform infrared spectroscopy (FT-IR).²⁸

The structure of **1** contains only one building unit of TCPP. As displayed in Fig. 1a, four carboxyl groups from four different TCPP molecules form three intermolecular O-H \cdots O hydrogen bonds, which can be viewed as a linkage node, termed LA. Each LA connects to four TCPP units, and each TCPP links with four LA units, extending into a (4, 4)-connected two-dimensional (2D) layer with rhombic cavities (Fig. 1b). The 2D layers are further packed together in an ABAB fashion through continuously offset π - π interactions between adjacent porphyrin rings with an interlayer separation of 3.6 Å (Fig. 1c-e) and edge-to-face π - π interactions between neighboring benzene rings (Fig. S6[†]). This generates a porous network with rhombic

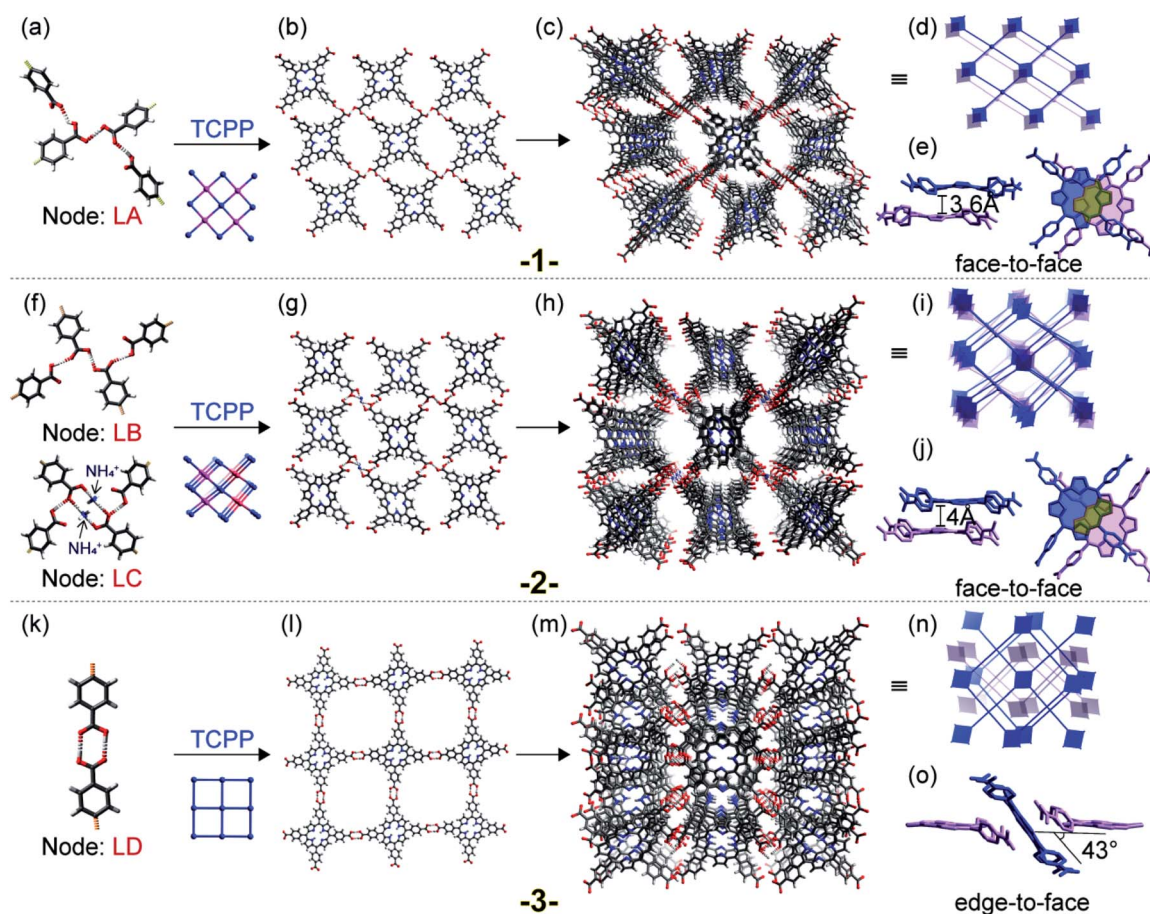


Fig. 1 Assembly of **1** (a–e), **2** (f–j) with face-to-face π - π interactions, and **3** (k–o) with edge-to-face π - π interactions between neighbouring porphyrin macrocycles. C, N, O, and H are depicted in gray, blue, red, and white, respectively.

channels of *ca.* 11.5×16.2 Å along the direction of the crystallographic *a*-axis (Fig. 1c).

The structure of **2** is quite different from that of **1**. It crystallizes in the monoclinic $P2_1/n$ space group (Table S1†) and possesses two types of linkage nodes, termed LB and LC (Fig. 1f). The LB node is similar to the LA node in **1**, and is composed of three O–H⋯O hydrogen bonds from four carboxyl groups. But the LC unit in **2** is built of two O–H⋯O hydrogen bonds and four N–H⋯O involving four carboxyl groups and two lattice ammonium ions. Ammonium ions should come from the decomposition of DMF. The LB and LC nodes are spatially linked through TCPP forming a 3D framework and leaving elliptical channels with approximate dimensions of 10.1×14.6 Å (Fig. 1h). If the H-bonding units (LB and LC) and the TCPP moieties are treated as 4-connected nodes, the structure of **2** can be simplified into a two-fold interpenetrated uninodal net with a Schläfli symbol of $\{8^6\}$ (Fig. 1i). The offset face-to-face π – π interactions between porphyrin rings from the two interpenetrated nets are present in **2** with a separation of 4.0 Å, greater than that in **1**. The overlap degree of two π – π associated porphyrin rings in **2** is also lower than that in **1** (Fig. 1j).

Compound **3** crystallizes in the orthogonal space group $Cmce$ and has a periodic 2D net. Different from those in **1** and **2**, the linkages between TCPP in **3** are two intermolecular –COOH⋯HOOC– hydrogen bonds with an O⋯O separation of 2.602 Å. In **1** and **2**, the O⋯O distance associated with the hydrogen bonds is 2.539 to 2.636 Å in the range of strong hydrogen bonds. In **3**, however, the 2D sheets are interlocked in a 3D space. The short contacts between the interpenetrating layers of **3** are not conducive to the formation of π – π or p– π interactions between the adjacent aromatic rings, and they also lead to pore blocking.

As shown in Fig. S4,† the flexibility of the hydrogen bonding nodes A, B and C allows the formation of an eclipsed array of porphyrin rings with face-to-face π – π interactions. Four benzoic groups associated with node A in **1** twist to a greater extent than those with nodes B and C in **2**. In view of the deflection angle of $>35^\circ$ between the four planes of the benzoic groups and the porphyrin ring in TCPP, all the porphyrin rings are approximately coplanar in **1**, and form a 2D layered structure, while in **2**, the porphyrin rings are unable to be coplanar and this leads to the fabrication of a 3D network structure. As shown in Fig. S5,† the nodes of LB and LC are connected to each other forming a chain with weaker hydrogen bonding (N⋯O distances of 2.91–2.94 Å). Accordingly, the structure of **2** can also be viewed as a (4, 6)-connected net, another novel topological framework with a Schläfli symbol of $[6^{11} \cdot 8^4][6^6]$. The connection node D in **3** is relatively rigid, which limits further twisting, and does not support the close stacking of adjacent porphyrin rings through π – π interactions.

The PXRD patterns of experimental **1**, **2** and **3** matched well with the simulated patterns (Fig. 2a and S2†). As depicted in Fig. 2b and S8,† there is no crystallinity loss or phase change below 150 °C for **1** and 90 °C for **2**. It is worth noting that the PXRD of compound **2** changed significantly after 90 degrees, which is due to the phase transition caused by temperature. **1** or **2** can maintain its structural integrity after soaking the sample in water and solvents, such as acetone, dichloromethane,

toluene, acetonitrile, and *n*-hexane for at least 12 h (Fig. S9†). The thermogravimetric analysis (TGA) curves of **1** and **2** showed that TCPP is stable up to 400 °C (Fig. S7†). Before that, there are several weight loss steps, which may correspond to the evaporation of the solvent. The permanent porosities of the activated **1** and **2** were confirmed by N₂ sorption experiments. The Brunauer–Emmett–Teller (BET) surface areas of **1** and **2** were calculated to be 718 and 499 m² g^{−1}, respectively (Fig. 2c). The calculated pore sizes, 11.7 Å for **1** and 11.5 Å for **2**, are close to the values determined from their crystal structures (Fig. 2c inset). The solvent-accessible void spaces of **1** and **2** calculated by PLATON analysis are 699.2 and 1282.0 Å³ per cell, respectively.

The UV-Vis spectra (Fig. 2d) of the samples showed an absorption onset at about 800 nm. The Tauc plot derived from the spectra of **1**, **2**, and **3** yielded bandgaps of *ca.* 1.72, 1.73, and 1.71 eV, respectively. Conductivity measurements were performed with pressed pellets of the samples by the standard two-contact probe method.^{29,30} As shown in Fig. 2e, f and S10,† the room temperature conductivities (σ) of **1**, **2** and **3** were 2.02×10^{-12} , 3.26×10^{-12} and 2.15×10^{-13} S cm^{−1}, respectively. The conductivity increased upon raising the temperature, which further demonstrates their semiconducting nature. At 120 °C, the σ values of **1**, **2** and **3** are 1.07×10^{-9} , 2.40×10^{-9} and 2.84×10^{-11} S cm^{−1}, respectively.

The combination of porosity and semiconducting properties of **1** and **2** allows their application in electronic devices, such as chemiresistive sensors for NO₂ detection. The linear *I*–*V* curve indicated good ohmic contact between the sensing material and electrodes (Fig. S11†). The gas sensing experiments were carried out by placing the sensors in a sealed quartz chamber, and then monitoring the current change upon cyclic exposure to analytic gases and dry air (Fig. S12†). **1** showed high sensitivity with a response of $1.8 \times 10^5\%$ toward 100 ppm NO₂, but could not fully recover in the dark, which resulted in a decrease of the sensitivity upon repeated assays (Fig. 3a). Under visible light, the response–recovery was a desired reversible process (Fig. 3b and S13†), for the light improved desorption processes (Fig. S14†). It's worth mentioning that **1** maintained a response value as high as $1.7 \times 10^5\%$ toward 100 ppm NO₂ (Fig. 3b). It is

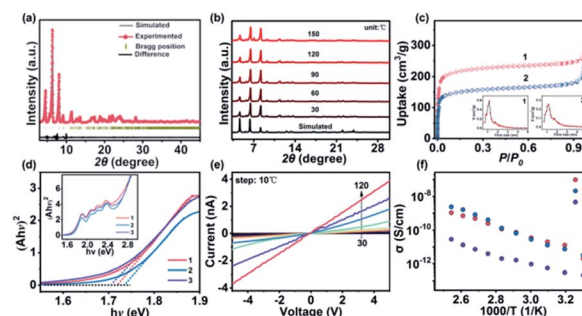


Fig. 2 (a) PXRD patterns of **1**; (b) various temperature PXRD patterns of **1**; (c) N₂ adsorption isotherms and pore size distribution of **1** and **2** (77 K); (d) solid-state UV-Vis spectra of **1**, **2** and **3**; (e) temperature-dependent *I*–*V* curves of **1**; (f) variable temperature conductivities of **1**, **2** and **3**.

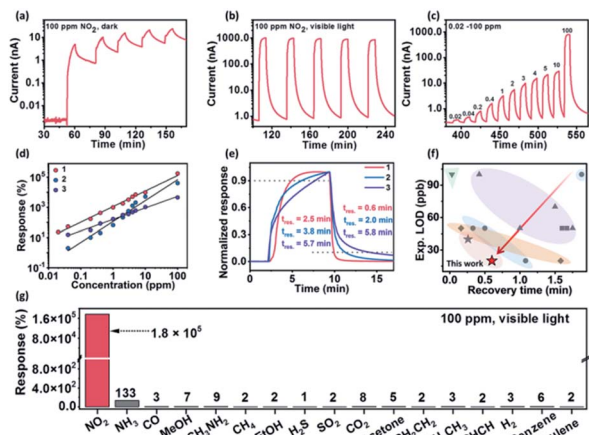


Fig. 3 NO_2 gas sensing properties of **1**, **2** and **3** at rt: dynamic response–recovery curve of **1** to 100 ppm NO_2 for five successive assays (a) in the dark and (b) under visible light; (c) dynamic response–recovery curve of **1** to NO_2 with different concentrations; (d) log–log plots of response–concentration of **1**, **2** and **3**; (e) response–recovery times of **1**, **2** and **3** to 100 ppm NO_2 ; (f) exp. LOD and recovery time comparison of various NO_2 sensing at rt (l, metal–sulfide; \blacktriangle , MOX; \blacktriangledown , graphene; n, organic compounds; u, reduced graphene oxide; \star : HOF)^{23,31–44} (g) response comparison of **1** among NO_2 and interference gases.

credited that light illumination can promote the separation of electron–hole pairs and realize the improvement of photocurrent (Fig. S15[†]). The above process can effectively increase the concentration of the reactive oxygen (O_2^- or O_2^{2-}), which is a key active species for sensing reaction. With 100 ppm NO_2 , **1** was examined in five successive assays and had a coefficient of variation (CV) of 6%, indicating good repeatability.

When exposed to NO_2 of incremental concentration (0.02–100 ppm), **1**, **2** and **3** showed a continuously increased response (Fig. 3c and S16[†]). Compared with **2** and **3**, **1** exhibited a much superior sensing performance (Fig. 3d). Upon exposure to 100 ppm NO_2 , **2** and **3** have lower responses of $\sim 4.0 \times 10^4\%$ and $4.5 \times 10^3\%$, respectively, which are 4.3 and 37.8 times lower than that of **1**. Compared with non-porous **3**, porous **1** exhibited as high as 37.8 times enhanced response value indicating the necessity of porosity in gas sensing behavior. Notably, **1** also showed a 54 times higher response than the reported microporous OSMS.²³ Their log–log plots of response *vs.* concentration displayed good linearity (Fig. 3d). Accordingly, the theoretical Limits of Detection (LOD) of **1**, **2**, and **3** were deduced to be 8, 171, and 28 ppb, respectively, by setting the response to 10%.²⁶ Experimentally, **1** showed a noticeable response at a concentration as low as 20 ppb, which is lower than the safety limit of annual exposure (109.6 ppb) set by the World Health Organization. The response and recovery time of **1** to 100 ppm NO_2 were estimated to be 2.5 and 0.6 min (Fig. 3e), respectively. **2** and **3** showed longer response and recovery times (3.8 and 2.0 min for **2**; 5.7 and 5.8 min for **3**, respectively) (Fig. 3e). Notably, due to the strong interaction between NO_2 and sensing materials, it is still a major challenge for rt NO_2 sensors to achieve a low experimental LOD and fast recovery

simultaneously (Table S4[†]). To the best of our knowledge, **1** with an experimental LOD as low as 20 ppb and a recovery time as short as 0.6 min (Fig. 3f) represents the first chemiresistive sensing material towards NO_2 with such high performance.

Due to the high sensitivity of **1**, its reproducibility was evaluated using 3 devices. The responses toward 100 ppm NO_2 are $1.52 \times 10^5\%$, $1.30 \times 10^5\%$ and $1.55 \times 10^5\%$, respectively (Fig. S17[†]), confirming its excellent reproducibility. The unique selectivity of **1** towards NO_2 was evaluated by measuring the response toward 16 typical interfering gases. As shown in Fig. 3g, S18 and S19,[†] **1** has a selectivity coefficient ($R_{\text{NO}_2}/R_{\text{interference}}$) ranging from ~ 1326 –176 455, indicating excellent selectivity. The sensor showed a selectivity coefficient as high as 17 645–58 toward 40–80% RH and noticeable long-term stability (Fig. S20–S22[†]).

FT-IR spectroscopy was performed to further understand the origin of the excellent performance of **1** (Fig. 4a). It was found that after exposure to 100 ppm NO_2 for 2 h at rt in a dark atmosphere, **1** showed several new peaks in its spectra. The new peaks at 1562 and 1382 cm^{-1} belong to monodentate nitrate and nitrito complexes.⁴⁵ The band at 1665 cm^{-1} is related to asymmetric stretching vibrations of adsorbed NO_2 ,⁴⁶ and the peak at 2425 cm^{-1} may be due to the N=O vibration of nitrosonium NO^+ .⁴⁷ These peaks clearly demonstrate the successful adsorption of NO_2 by **1**. The peak intensity at ~ 3127 cm^{-1} corresponding to the –NH vibration decreased dramatically.⁴⁸ The $-\text{C}_2\text{N}$ peak at 1397 cm^{-1} and the –NH peaks at 1582 and 1534 cm^{-1} become weaker, suggesting that the N on the porphyrin ring is possibly the active site of NO_2 adsorption.

According to the above results, a possible NO_2 sensing mechanism was proposed and is shown in Fig. 4b. First, as shown in Fig. 3a–c, it shows a positive current response upon exposure of **1** to NO_2 , suggesting a p-type semiconductor behavior. When NO_2 was introduced onto the surface of **1**, the strong electron acceptor NO_2 could be rapidly adsorbed on the N active site of **1**. The oxidation of NO_2 by adsorbed reactive

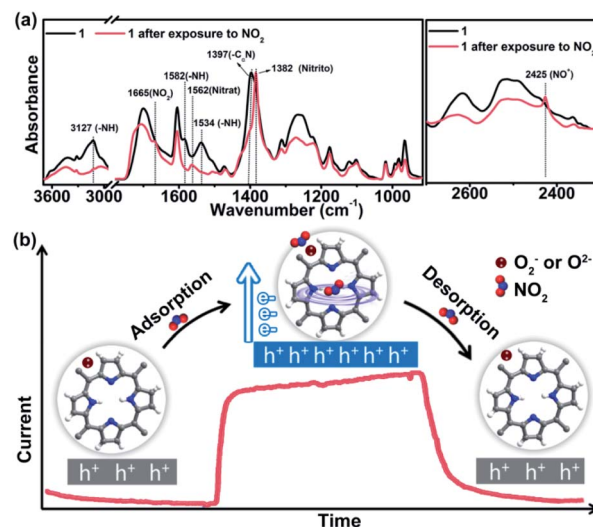


Fig. 4 (a) FT-IR spectra and (b) the possible NO_2 sensing mechanism for **1**.

oxygen (O_2^- or O^{2-}) or reduction of NO_2 by the electron rich porphyrin ring formed nitrite and nitrito species (eqn (1)–(4), ESI^\dagger).^{23,45,47} Meanwhile, the electron concentration of **1** decreases and the hole concentration increases, which remarkably increases the conductivity of p-type semiconductor **1** and produces the sensing response. Once NO_2 was removed from the surface of **1** with the assistance of visible light, the trapped electrons are released back to **1**, causing the current recovery in **1**.

Conclusion

Aiming to create microporous OSMS materials and improve their mass and charge transport properties, the relationship among the hydrogen bonding linkage, packing structure and sensing performances has been carefully studied. It is found that the aggregate of hydrogen bonds among porphyrin molecules acts as linkage nodes and plays a critical role in determining the long-range packing structure in crystals and producing permanent porosity. Three different types of linkage nodes were found in our prepared OSMS crystals (**1**, **2**, and **3**). Varying the structure of the linkage nodes substantially changed the packing mode of porphyrins, which results in different intermolecular interactions, geometries and stabilities of the pores. The highly flexible LA linkage node endowed the porphyrin OSMS with the highest porosity, the largest overlap of porphyrin rings, and the strongest face-to-face π - π interaction. With the excellent mass and charge transport pathway, **1** was studied as a rt chemiresistive gas sensing material for NO_2 . It shows one of the highest comprehensive performances among all reported rt sensing materials with experimental LOD < 20 ppb, recovery time < 0.6 min, response value > $1 \times 10^5\%$, and exceptional selectivity toward 16 interfering gases. This work revealed that the aggregate of hydrogen bonds is a useful tool for designing and controlling the packing structure of OSMSs to achieve better mass and charge transport pathways.

Experimental

Materials and general methods

Chemicals. All chemical reagents and solvents were obtained from commercial suppliers and used without further purification.

Characterization. Powder X-ray diffraction (PXRD) was carried out with a Rigaku Dmax 2500 X-ray diffractometer with a Cu sealed tube ($\lambda = 1.54178 \text{ \AA}$). Variable temperature XRD was carried out with a Rigaku, Ultima-IV Desktop X-ray diffractometer. Elemental analysis (EA) was carried out on a Vario EL-Cube. Fourier-transform infrared (FT-IR) spectroscopy was performed in the range $4000\text{--}400 \text{ cm}^{-1}$ using KBr pellets on a Nicolet Magna 750 FT-IR spectrometer. Thermogravimetric analysis (TGA) of the samples was performed using a Netzsch STA449C thermal analyzer in a temperature range of 25 to $800 \text{ }^\circ\text{C}$ under a N_2 atmosphere with a heating rate of $10 \text{ }^\circ\text{C min}^{-1}$. Field emission scanning electron microscopy (FE-SEM) images were obtained with a JSM6700-F microscope. Ultraviolet-visible diffuse reflectance spectroscopy (UV-Vis DRS)

was performed on a PerkinElmer Lambda 950 UV-Vis spectrophotometer from 250 to 800 nm using BaSO_4 as a standard with 100% reflectance. N_2 sorption measurements were conducted using a Micromeritics ASAP 2020 system.

Synthetic procedures

Synthesis of **1**

A mixture of TCPP (tetrakis(4-carboxylphenyl)porphyrin) (10 mg) and BA (benzoic acid) (100 mg) was added into a solution of DMF (*N,N*-dimethylformamide) (1 mL) and MeCN (3 mL), sealed in a 23 mL autoclave, heated at $120 \text{ }^\circ\text{C}$ for 24 h, and then cooled to room temperature (rt) to give long red-brown crystals. Anal. calcd (%): C, 72.84; H, 3.79; N, 7.08; O, 16.19%. Found (%): C, 66; H, 4.74; N, 8.47; O, 21.10.

Synthesis of **2**

The synthetic conditions of **2** are similar to those of **1**, except for using a temperature of $160 \text{ }^\circ\text{C}$. Anal. calcd (%): C, 61.63; H, 5.085; N, 8.628; O, 24.65%. Found (%): C, 65.97; H, 4.83; N, 8.42; O, 20.42.

Synthesis of **3**

The synthetic conditions of **3** are similar to those of **1**, except for using a temperature of $60 \text{ }^\circ\text{C}$. Anal. calcd (%): C, 72.84; H, 3.79; N, 7.08; O, 16.19%. Found (%): C, 66.20; H, 4.83; N, 8.41; O, 20.44.

Crystallographic data

Single crystals of **2** were carefully selected under an optical microscope and glued to a thin glass fiber. Single-crystal XRD data were collected on a ROD, Synergy Custom system, HyPix diffractometer equipped with Ga K_α ($\lambda = 1.34050 \text{ \AA}$) radiation at rt. The data integration and reduction were processed with the CrysAlisPro (Rigaku Oxford Diffraction) program of the software. A multi-scan absorption correction was applied to the collected reflections. The structure was solved with the SHELXT structure solution program and was refined on F^2 by a full-matrix least-squares technique using the SHELXL program package. All the non-hydrogen atoms are refined anisotropically and hydrogen positions were fixed at calculated positions and refined isotropically. We employed OLEX2/SOLVENT MASK to calculate the diffraction contribution of the solvent molecules and thereby, to produce a set of solvent-free diffraction intensities. With the solvent mask, 278 electrons were found in a void volume of 1218 \AA^3 in 1 per unit cell, which is consistent with the presence of $7[\text{H}_2\text{O}]$ per asymmetric unit.

Evaluation of electronic conductivity

The conductivity of the powder pellets (**1**, **2** and **3**) was measured by a two-contact probe method on a semiconductor analysis system (Keithley 4200). First, 5/5/7 mg of each powder sample (**1**, **2** and **3**) was pressed into cylindrical pellets at a pressure of ca. 0.3 GPa with a diameter of 0.25 cm and a thickness of $\sim 0.067/0.072/0.094 \text{ cm}$, respectively. Then, the round surfaces

of the pellets were covered by silver paste and connected to the 4200 analyzers *via* gold wires (diameter, 50 μm). The variable temperature electrical measurements were performed using a Lakeshore probe station. The electrical conductivity, σ (S cm^{-1}), was calculated based on Ohm's law by fitting the linear region of the current–voltage curves.

The UV-Vis spectrum was recorded for calculation of the bandgaps using the Tauc plot method. The Tauc plot is mainly based on the formula proposed by Tauc, Davis and Mott *et al.* $(\alpha h\nu)^{1/n} = B(h\nu - E_g)$, where α is the absorption coefficient, h is the Planck constant, ν is the frequency, B is the constant, E_g is the bandgap width of the semiconductor, and exponential n is directly related to the type of semiconductor, direct bandgap $n = 1/2$, indirect bandgap $n = 2$. In this manuscript, when $n = 1/2$, the Tauc plot derived from the spectra of **1** yielded bandgaps of *ca.* 1.72 eV, respectively. Meanwhile, it is also common to use the activation energy to derive the fundamental band gap (E_g) by applying the formula $E_g = 2E_a$, where E_a is the energy difference between the valence band maximum and the conduction band minimum. As shown in Fig. 2f, the activation energy (E_a) is typically obtained by fitting temperature-dependent conductivity data to the Arrhenius equation:

$$\sigma = \sigma_0 \exp\left(-\frac{E_a}{kT}\right)$$

where σ_0 is a prefactor. The calculated E_a for compound **1** is 0.7 eV. The corresponding E_g is 1.4 eV. This value was consistent with the value of the Tauc plot derived E_g , which indicates that these materials are direct bandgap semiconductors.

Evaluation of sensing performance

The light source for gas sensing tests was a 300 W Xe lamp with a cut-off filter ($420 \text{ nm} < \lambda < 790 \text{ nm}$) and the power density can be tuned by changing the current running through it. Electrical characterization and resistance change during gas injection were recorded with a Keithley 2602B semiconductor characterization system. Pristine **1**, **2** and **3** gas sensors were fabricated through a drop-casting method. 0.2 mL of **1**, **2** or **3** water solution (5 mg mL^{-1}) was dropped on the surface of the Ag interdigitated electrode (10 pairs of digits with 5 μm fingers and 15 μm gaps, Synkera), followed by drying in air for 12 h to form a sensing layer. The interdigitated electrode was connected *via* a Keithley 2602B source meter for sensing testing. Conductive silver paint (SPI# 05002-AB, Structure Probe, Inc. 206 Garfield Ave, West Chester, PA 19380-4512) was used to build the ohmic contact between the sensing film and two Au wires on both ends of the substrate. The sensor characterization was conducted using a home-made system in a sealed gas-sensing chamber. Dry air (21% O_2 and 79% N_2) was used as the purging gas. The target gas (Beijing Hua Yuan Gas Chemical Industry Co., Ltd., China) concentration was controlled by dilution with dry air and introduced into the quartz tube. Mass flow controllers (CS-200C, Beijing Sevenstar Qualiflow Electronic Equipment Manufacturing Co., Ltd., China) were used to control the concentration. It takes ~ 1.3 min to fulfill the quartz chamber when the total flow rate was 600 sccm. The current was recorded

using a Keithley 2602B Sourcemeater, and the bias on the sensor was fixed at 5 V. The gas response is defined as the ratio of sensor resistance in air (R_{air}) and in analytic gas (R_{analyte}): response = $R_{\text{analyte}}/R_{\text{air}} - 1$ (reducing gas) or response = $R_{\text{air}}/R_{\text{analyte}} - 1$ (oxidizing gas). The gas selectivity to NO_2 is defined as the ratio of sensor response in analytic gas (R_{analyte}) and in interfering gas ($R_{\text{interfering}}$). The response time of the sensor is the time required for increasing (or decreasing) the current to 90% of the saturation value and the recovery time is the time required for decreasing (or increasing) the saturated current to its 10%. The coefficient of variation (CV) is used to represent the repeatability of our sensing devices, which is defined as: $\text{CV} = R_{\text{SD}}/R_{\text{average}} \times 100\%$, where R_{SD} and R_{average} are the standard deviation (SD) and average value of responses with five successive cycles.

Author contributions

G. Xu and Q. P. Lin proposed and supervised the project. G. Xu, Q.P. Lin, W. H. Deng and L. He conceived and designed the experiments. L. He and Q.P. Lin performed the synthesis and structure refinements. W. H. Deng, and G. Xu performed the sensing experiments, conductivity measurements, mechanism exploration and structure-relationship analysis. L. He performed the PXRD, FT-IR, UV, TGA and Gas sorption analyses. G. Xu, Q. P. Lin, W. H. Deng, L. He wrote the manuscript. All authors analyzed the data and commented on the manuscript.

Conflicts of interest

There are no conflicts to declare.

Acknowledgements

This work was supported by the NSF of China (21822109, 21805276, 21975254, 22175176, 91961115, and 22171263), International Partnership Program of CAS (121835KYSB20180037), the NSF of Fujian (2021J02017, 2020J01109), Youth Innovation Promotion Association CAS, and Fujian Science & Technology Innovation Laboratory for Optoelectronic Information of China (2021ZR101 and 2021ZR138).

References

- 1 Y. Lin, Y. Li and X. Zhan, *Chem. Soc. Rev.*, 2012, **41**, 4245–4272.
- 2 Y. Wang, L. Sun, C. Wang, F. Yang, X. Ren, X. Zhang, H. Dong and W. Hu, *Chem. Soc. Rev.*, 2019, **48**, 1492–1530.
- 3 H. Guo, C.-Y. Yang, X. Zhang, A. Motta, K. Feng, Y. Xia, Y. Shi, Z. Wu, K. Yang, J. Chen, Q. Liao, Y. Tang, H. Sun, H. Y. Woo, S. Fabiano, A. Facchetti and X. Guo, *Nature*, 2021, **599**, 67–73.
- 4 S. Motoyama, R. Makiura, O. Sakata and H. Kitagawa, *J. Am. Chem. Soc.*, 2011, **133**, 5640–5643.
- 5 I. Nasrallah, M. K. Ravva, K. Broch, J. Novak, J. Armitage, G. Schweicher, A. Sadhanala, J. E. Anthony, J.-L. Bredas and H. Sirringhaus, *Adv. Electron. Mater.*, 2020, **6**, 2000250.

- 6 H. Bin, J. Wang, J. Li, M. M. Wienk and R. A. J. Janssen, *Adv. Mater.*, 2021, **33**, 2008429.
- 7 T. P. Nguyen, A. D. Easley, N. Kang, S. Khan, S.-M. Lim, Y. H. Rezenom, S. Wang, D. K. Tran, J. Fan, R. A. Letteri, X. He, L. Su, C.-H. Yu, J. L. Lutkenhaus and K. L. Wooley, *Nature*, 2021, **593**, 61–66.
- 8 A. J. Sneyd, T. Fukui, D. Palecek, S. Prodhan, I. Wagner, Y. Zhang, J. Sung, S. M. Collins, T. J. A. Slater, Z. Andaji-Garmaroudi, L. R. MacFarlane, J. D. Garcia-Hernandez, L. Wang, G. R. Whittell, J. M. Hodgkiss, K. Chen, D. Beljonne, I. Manners, R. H. Friend and A. Rao, *Sci. Adv.*, 2021, **7**, eabh4232.
- 9 Z. Qin, H. Gao, H. Dong and W. Hu, *Adv. Mater.*, 2021, **33**, 2007149.
- 10 S. Fratini, M. Nikolka, A. Salleo, G. Schweicher and H. Sirringhaus, *Nat. Mater.*, 2020, **19**, 491–502.
- 11 Y. Lu, Z.-D. Yu, H.-I. Un, Z.-F. Yao, H.-Y. You, W. Jin, L. Li, Z.-Y. Wang, B.-W. Dong, S. Barlow, E. Longhi, C.-a. Di, D. Zhu, J.-Y. Wang, C. Silva, S. R. Marder and J. Pei, *Adv. Mater.*, 2021, **33**, 2005946.
- 12 X. Liu, G. Zhu, D. He, L. Gu, P. Shen, G. Cui, S. Wang, Z. Shi, D. Miyajima and S. Wang, *CCS Chem.*, 2021, **3**, 2473–2481.
- 13 H. Bin, Y. Yang, Z.-G. Zhang, L. Ye, M. Ghasem, S. Chen, Y. Zhang, C. Zhang, C. Sun, L. Xue, C. Yang, H. Ade and Y. Li, *J. Am. Chem. Soc.*, 2017, **139**, 5085–5094.
- 14 B. Kang, M. Jang, Y. Chung, H. Kim, S. K. Kwak, J. H. Oh and K. Cho, *Nat. Commun.*, 2014, **5**, 4752.
- 15 X. Zhang, B. Wang, L. Huang, W. Huang, Z. Wang, W. Zhu, Y. Chen, Y. Mao, A. Facchetti and T. J. Marks, *Sci. Adv.*, 2020, **6**, eaaz1042.
- 16 Q. Wang, S. Wu, F. Ge, G. Zhang, H. Lu and L. Qiu, *Adv. Mater. Interfaces*, 2016, **3**, 1600518.
- 17 R. B. Lin, Y. He, P. Li, H. Wang, W. Zhou and B. Chen, *Chem. Soc. Rev.*, 2019, **48**, 1362–1389.
- 18 X. Zhang, L. Li, J.-X. Wang, H.-M. Wen, R. Krishna, H. Wu, W. Zhou, Z.-N. Chen, B. Li, G. Qian and B. Chen, *J. Am. Chem. Soc.*, 2020, **142**, 633–640.
- 19 S. Feng, Y. Shang, Z. Wang, Z. Kang, R. Wang, J. Jiang, L. Fan, W. Fan, Z. Liu, G. Kong, Y. Feng, S. Hu, H. Guo and D. Sun, *Angew. Chem., Int. Ed.*, 2020, **59**, 3840–3845.
- 20 Y.-L. Li, E. V. Alexandrov, Q. Yin, L. Li, Z.-B. Fang, W. Yuan, D. M. Proserpio and T.-F. Liu, *J. Am. Chem. Soc.*, 2020, **142**, 7218–7224.
- 21 A. Karmakar, R. Illathvalappil, B. Anothumakkool, A. Sen, P. Samanta, A. V. Desai, S. Kurungot and S. K. Ghosh, *Angew. Chem., Int. Ed.*, 2016, **55**, 10667–10671.
- 22 Y.-R. Wang, M. Liu, G.-K. Gao, Y.-L. Yang, R.-X. Yang, H.-M. Ding, Y. Chen, S.-L. Li and Y.-Q. Lan, *Angew. Chem., Int. Ed.*, 2021, **60**, 21952–21958.
- 23 Y. Wang, D. Liu, J. Yin, Y. Shang, J. Du, Z. Kang, R. Wang, Y. Chen, D. Sun and J. Jiang, *Chem. Commun.*, 2020, **56**, 703–706.
- 24 W.-T. Koo, J.-S. Jang and I.-D. Kim, *Chem*, 2019, **5**, 1938–1963.
- 25 H. Yuan, S. A. A. Aljneibi, J. Yuan, Y. Wang, H. Liu, J. Fang, C. Tang, X. Yan, H. Cai, Y. Gu, S. J. Pennycook, J. Tao and D. Zhao, *Adv. Mater.*, 2019, **31**, 1807161.
- 26 M.-S. Yao, W.-X. Tang, G.-E. Wang, B. Nath and G. Xu, *Adv. Mater.*, 2016, **28**, 5229–5234.
- 27 X. Qu, H. Zhang, D. Yu, S. Liu, C. Liu, Z. Liu and J. Ren, *Angew. Chem., Int. Ed.*, 2021, **60**, 2–12.
- 28 K. Hayashi, M. Nakamura, H. Miki, S. Ozaki, M. Abe, T. Matsumoto and K. Ishimura, *Adv. Funct. Mater.*, 2012, **22**, 3539–3546.
- 29 Y. Li, X. Jiang, Z. Fu, Q. Huang, G.-E. Wang, W.-H. Deng, C. Wang, Z. Li, W. Yin, B. Chen and G. Xu, *Nat. Commun.*, 2020, **11**, 261.
- 30 C.-P. Wang, K. Chiranjeevulu, X.-L. Ye, W.-H. Li, E. Wang Guan and G. Xu, *Chin. J. Struct. Chem.*, 2021, **40**, 1138–1144.
- 31 Z. Wang, T. Zhang, C. Zhao, T. Han, T. Fei, S. Liu and G. Lu, *J. Colloid Interface Sci.*, 2018, **514**, 599–608.
- 32 B. Liu, Y. Luo, K. Li, H. Wang, L. Gao and G. Duan, *Adv. Mater. Interfaces*, 2019, **6**, 1900376.
- 33 A. Giampiccolo, D. M. Tobaldi, S. G. Leonardi, B. J. Murdoch, M. P. Seabra, M. P. Ansell, G. Neri and R. J. Ball, *Appl. Catal., B*, 2019, **243**, 183–194.
- 34 T. Wu, Z. Wang, M. Tian, J. Miao, H. Zhang and J. Sun, *Sens. Actuators, B*, 2018, **259**, 526–531.
- 35 Y. Zhou, C. Gao and Y. Guo, *J. Mater. Chem. A*, 2018, **6**, 10286–10296.
- 36 J. Guo, R. Wen, J. Zhai and Z. L. Wang, *Sci. Bull.*, 2019, **64**, 128–135.
- 37 W. Jiang, T. Wang, X. Chen, B. Li, M. Zeng, N. Hu, Y. Su, Z. Zhou, Y. Zhang and Z. Yang, *Phys. Chem. Chem. Phys.*, 2020, **22**, 18499–18506.
- 38 W. Jiang, X. Chen, T. Wang, B. Li, M. Zeng, J. Yang, N. Hu, Y. Su, Z. Zhou and Z. Yang, *RSC Adv.*, 2021, **11**, 5618–5628.
- 39 C. Gomez-Navarro, R. T. Weitz, A. M. Bittner, M. Scolari, A. Mews, M. Burghard and K. Kern, *Nano Lett.*, 2009, **7**, 3499–3503.
- 40 J. Wu, Z. Wu, H. Ding, X. Yang, Y. Wei, M. Xiao, Z. Yang, B.-R. Yang, C. Liu, X. Lu, L. Qiu and X. Wang, *ACS Sens.*, 2019, **4**, 1889–1898.
- 41 J. Wu, S. Feng, X. Wei, J. Shen, W. Lu, H. Shi, K. Tao, S. Lu, T. Sun, L. Yu, C. Du, J. Miao and L. K. Norford, *Adv. Funct. Mater.*, 2016, **26**, 7462–7469.
- 42 H.-Y. Li, J.-W. Yoon, C.-S. Lee, K. Lim, J.-W. Yoon and J.-H. Lee, *Sens. Actuators, B*, 2018, **255**, 2963–2970.
- 43 L. S. Chia, Y. H. Du, S. Palale and P. S. Lee, *ACS Omega*, 2019, **4**, 10388–10395.
- 44 L. Liu, M. Ikram, L. Ma, X. Zhang, H. Lv, M. Ullah, M. Khan, H. Yu and K. Shi, *J. Hazard. Mater.*, 2020, **393**, 122325–122335.
- 45 E. Ozensoy, D. Herling and J. Szanyi, *Catal. Today*, 2008, **136**, 46–54.
- 46 L. Yang, A. Marikutsa, M. Rumyantseva, E. Konstantinova, N. Khmelevsky and A. Gaskov, *Sensors*, 2019, **19**, 3405.
- 47 K. I. Hadjiivanov, *Catal. Rev.*, 2000, **42**, 71–144.
- 48 N. Dattagupta and T. J. Bardos, *J. Heterocycl. Chem.*, 1966, **3**, 495–502.